View metadata, citation and similar papers at core.ac.uk
brought to you by CORE
provided by Kanazawa University Repository for Academic Resources

Visualizing Nanoscale Distribution of Corrosion Cells by Open-Loop Electric Potential Microscopy

著者	Honbo Kyoko, Ogata Shoichiro, Kitagawa Takuya, Okamoto Takahiro, Kobayashi Naritaka, Sugimoto Itto, Shima Shohei, Fukunaga Akira, Takatoh Chikako, Fukuma Takeshi
journal or publication title	ACS Nano
volume	10
number	2
page range	2575-2583
year	2016-02-23
URL	http://hdl.handle.net/2297/45479

doi: 10.1021/acsnano.5b07552

1
2
3
4
5
6
7
8
9
10
11
12
13
14
15
16
17
18
19
20
21
22
23
24
25
26
27
28
29
30
31
32
33
34
35
36
37
38
39
40
41
42
43
44
45
46
47
48
49
50
51
52
53
54
55
56
57
58
59
60

Visualizing Nanoscale Distribution of Corrosion Cells by Open-Loop Electric Potential Microscopy

Kyoko Honbo,[†,‡] Shoichiro Ogata,[†,‖] Takuya Kitagawa,[†] Takahiro Okamoto,[†] Naritaka Kobayashi,[†,⊥] Itto Sugimoto,[‡] Shohei Shima,[¶] Akira Fukunaga,[¶] Chikako Takatoh,[¶] and Takeshi Fukuma[*,†,§]

Division of Electrical Engineering and Computer Science, Kanazawa University, Kakuma-machi, 920-1192 Kanazawa, Japan, Research and Development Group, Center for Technology Innovation - Materials, Hitachi, Ltd., 319-1292 Hitachi, Japan, EBARA Corporation, 144-8510 Tokyo, Japan, and ACT-C, Japan Science and Technology Agency, Honcho 4-1-9, 332-0012 Kawaguchi, Japan

E-mail: fukuma@staff.kanazawa-u.ac.jp

Abstract

Corrosion is a traditional problem but still one of the most serious problems in industry. To reduce the huge economic loss caused by corrosion, tremendous effort has been made to understand, predict and prevent it. Corrosion phenomena are generally explained by the formation of corrosion cells at a metal–electrolyte interface. However, experimental verification of their nanoscale distribution has been a major challenge

[*]To whom correspondence should be addressed
[†]Kanazawa University
[‡]Hitachi, Ltd.
[¶]EBARA Corporation
[§]JST
[‖]Present affiliation: EBARA Corporation, 144-8510 Tokyo, Japan
[⊥]Present affiliation: Saitama University, Saitama 338-8570, Japan

1
2
3
4
5
6
7
8
9
10
11
12
13
14
15
16
17
18
19
20
21
22
23
24
25
26
27
28
29
30
31
32
33
34
35
36
37
38
39
40
41
42
43
44
45
46
47
48
49
50
51
52
53
54
55
56
57
58
59
60

owing to the lack of a method able to visualize the local potential distribution in an electrolytic solution. In this study, we have investigated the nanoscale corrosion behavior of Cu fine wires and a duplex stainless steel by in-situ imaging of local corrosion cells by open-loop electric potential microscopy (OL-EPM). For both materials, potential images obtained by OL-EPM show nanoscale contrasts, where areas of higher and lower potential correspond to anodic areas (i.e., corrosion sites) and cathodic areas, respectively. This imaging capability allows us to investigate the real-time transition of local corrosion sites even when surface structures show little change. This is particularly useful for investigating reactions under surface oxide layers or highly corrosion-resistant materials as demonstrated here. The proposed technique should be applicable to the study of other redox reactions on a battery electrode or a catalytic material. The results presented here open up such future applications of OL-EPM in nanoscale electrochemistry.

Keywords: local corrosion cell, stainless steel, copper, open-loop electric potential microscopy, atomic force microscopy

Metal corrosion is a serious problem in many industrial fields.[1–5] Examples include the corrosion of stainless steel in nuclear power,[1] desalination[2] and chemical plants;[3] Cu fine wires in semiconducting devices;[4] and Al alloys in cars and robots.[5] Previous studies reported that the economic loss caused by corrosion typically amounts to 3–4% of GNP.[6] To reduce the economic loss, tremendous effort has been made to understand, predict and prevent corrosion.

Corrosion is the degradation of metals caused by the oxidation of surface atoms at a metal–water interface (the anodic area in Figure 1). This reaction leads to an increase in the density of cations (not necessarily metal ions) near the surface in the solution and the release of electrons into the metal electrode. For the continuous progress of the oxidation, the produced electrons should be transferred to another interfacial area where reduction takes place (the cathodic area in Figure 1). Typically, this corresponds to the reduction of O_2 or H^+, leading to an increase in the density of anions (e.g., OH^-) or a decrease in the density of

1
2
3
4
5
6
7
8
9
10
11
12
13
14
15
16
17
18
19
20
21
22
23
24
25
26
27
28
29
30
31
32
33
34
35
36
37
38
39
40
41
42
43
44
45
46
47
48
49
50
51
52
53
54
55
56
57
58
59
60

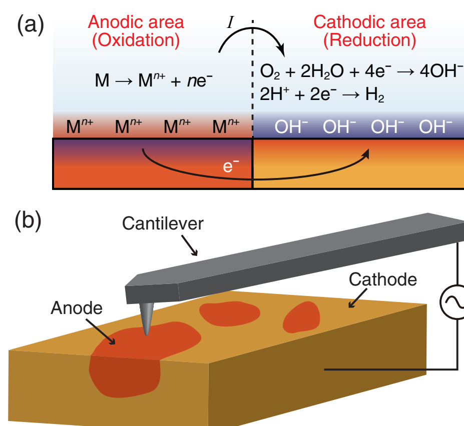

Figure 1: Schematic illustrations showing (a) typical corrosion reactions and (b) OL-EPM measurement of local corrosion cells.

cations (e.g., H^+) near the surface in the solution. The pairs of anodic and cathodic areas are referred to as corrosion cells and are considered to play a major role in corrosion processes.

The majority of previous corrosion studies were performed using electrochemical (EC) measurement techniques.[6] These previous works clarified the relationship between EC potential, current, time, temperature and solution conditions in various metal corrosion processes and thereby established a basic understanding of macroscopic corrosion behavior. Meanwhile, owing to the lack of locality in EC measurements, nanoscale corrosion behavior has been studied mainly using microscopy techniques. Electron microscopy has been used for ex-situ analyses of structural and compositional changes caused by corrosion.[7–14] Scanning tunneling microscopy (STM)[14,15] and atomic force microscopy (AFM)[9–11,16,17] have been used for ex-situ and in-situ analyses of nanoscale or atomic-scale structural changes in corrosion processes. Combined with EC measurement techniques, these methods have enabled macroscopic EC responses to be correlated with nanoscale corrosion behavior.

In spite of these efforts, the in-situ imaging of local corrosion cells has not been achieved. The formation of corrosion cells is one of the most fundamental and important concepts in corrosion science. It has often been postulated to explain many of the nanoscale corrosion behaviors. Therefore, the lack of a method able to experimentally verify their local distribu-

1
2
3
4
5
6
7
8
9
10
11
12
13
14
15
16
17
18
19
20
21
22
23
24
25
26
27
28
29
30
31
32
33
34
35
36
37
38
39
40
41
42
43
44
45
46
47
48
49
50
51
52
53
54
55
56
57
58
59
60

tion is a serious problem in corrosion science. In fact, this has critically limited our capability of studying the corrosion mechanism and evaluating local corrosion resistance.

For example, the corrosion of Cu in water is often driven by charge and material transfer through defects in a surface oxide layer between the solution and the underlying Cu electrode.[18,19] Under such a condition, structural changes at a surface appear only when the accumulated stress caused by corrosion reaches a certain level. Thus, real-time changes in corrosion sites are not necessarily able to be visualized by AFM or STM. This problem is particularly serious for evaluating the corrosion resistance of stainless steel. Owing to its high corrosion resistance, it often shows no surface structural changes within a typical experimental time (i.e., several hours). Practically, it is evaluated by immersing a metal piece in seawater for more than a few months. This requires considerable effort, cost and time but does not provide in-situ information.

To solve these problems, there has been strong demand for a tool for directly imaging local corrosion cells. In a corrosion process, a positive current flows from an anodic area to a cathodic area through a solution. Thus, the potential near an anodic area in a solution should be higher than that near a cathodic area. However, measurement of the nanoscale potential distribution in an electrolytic solution has been a major challenge.

So far, Kelvin probe force microscopy (KPFM) has been used for nanoscale or even atomic-scale surface potential measurements in air and vacuum.[20,21] In this method, ac and dc bias voltages ($V_{\mathrm{ac}} \cos \omega t$ and V_{dc}, respectively) are applied between a tip and a sample. The induced electrostatic force is detected and used to control V_{dc} such that the tip–sample potential difference is compensated. By recording V_{dc} during a lateral tip scan over a sample surface, we can map the distribution of local surface potential V_{s}. However, the application of a dc bias voltage induces uncontrolled EC reactions and the redistribution of ions, which prevent stable and reproducible measurements.

To overcome these difficulties, we have recently developed open-loop electric potential microscopy (OL-EPM).[22–24] In this method, only an ac bias voltage with a relatively high

ACS Paragon Plus Environment

frequency (ω) is applied between a tip and a sample so that we can avoid the aforementioned problems in KPFM. The induced cantilever vibrations with frequencies of ω and 2ω (A_1 and A_2, respectively) are detected and used to calculate local potential values. After the first proposal of this method,[22] a few research groups reported the same or similar methods using high-frequency ac bias modulation.[25–28]

Umeda *et al.* analyzed the distance dependence of the A_1 and A_2 signals using an equivalent circuit model of an electric double layer.[25,26] On the basis of the analyses, they proposed a method of estimating the surface potential value in water by fitting an equation to the measured distance dependence curves. Collins *et al.* proposed a method referred to as EC force microscopy for investigating the transient response of the A_1 signal induced by the application of a pulsed dc bias voltage.[27,28] They reported that the initial response of the A_1 signal shows quadratic dependence on the pulsed bias voltage in pure water. They proposed the estimation of the surface potential value from the bias voltage giving the minimum of the quadratic curve. While these previous works showed the possibility of surface potential measurements in pure water, they also pointed out significant difficulties in such measurements at the nanoscale or in an electrolytic solution. Therefore, the locality of the measured potential values, particularly in an electrolytic solution, and its correlation with interfacial EC processes such as corrosion have remained an open question.

In this study, we investigate the nanoscale structural and potential changes in Cu fine wires and stainless steel caused by corrosion in an electrolytic aqueous solution by OL-EPM. We discuss the correlation between the measured potential changes and the nanoscale corrosion behavior and present strong evidence for direct imaging of the nanoscale distribution of local corrosion cells. We also discuss the effectiveness of the obtained local information in understanding the nanoscale corrosion mechanism and evaluating the local corrosion resistance in industrial applications.

1
2
3
4
5
6
7
8
9
10
11
12
13
14
15
16
17
18
19
20
21
22
23
24
25
26
27
28
29
30
31
32
33
34
35
36
37
38
39
40
41
42
43
44
45
46
47
48
49
50
51
52
53
54
55
56
57
58
59
60

Results and Discussion

Corrosion of Cu fine wires

The corrosion of Cu fine wires is a serious problem in the semiconductor industry.[4,29] In the fabrication process of semiconductor devices, a Cu fine wire formed on a Si wafer is transiently exposed to a dilute electrolytic solution and partially dissolves to form nanoscale defects. To prevent such corrosion, it is crucial to understand its nanoscale origin, namely, where, when and how local corrosion cells are formed. In this study, we investigate the structural and potential changes in Cu fine wires on a Si wafer in dilute NaCl aqueous solution by OL-EPM.

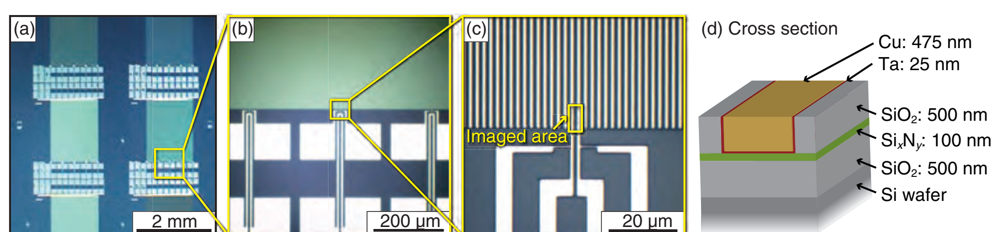

Figure 2: (a-c) Optical micrographs of Cu fine wires on a Si wafer. (d) Schematic illustration showing a cross section of a Cu fine wire.

Figure 2 shows optical micrographs of a sample used in this study. On the Si wafer, line and space patterns with different dimensions were formed (Figure 2a). In this study, we used two different patterns with line/space widths of 1 μm/1 μm and 2 μm/2 μm. Some of the wires were connected to a 100 μm $\times$ 100 μm pad as shown in Figure 2b. We imaged an area including two such wires by OL-EPM as indicated in Figure 2c. Figure 2d shows the cross-sectional structure of a Cu wire. Individual wires are electrically isolated by a SiO_2 layer. A 25 nm Ta layer was formed between the SiO_2 and Cu regions to improve the adhesion between the two materials as well as to prevent Cu diffusion into the SiO_2 region.

Figure 3 shows topographic and potential images of a 2 μm Cu wire obtained by OL-EPM in 10 μM NaCl solution. The bright regions on the left and right of the image correspond

1 2 3 4 5 6 7 8 9 10 11 12 13 14 15 16 17 18 19 20 21 22 23 24 25 26 27 28 29 30 31 32 33 34 35 36 37 38 39 40 41 42 43 44 45 46 47 48 49 50 51 52 53 54 55 56 57 58 59 60

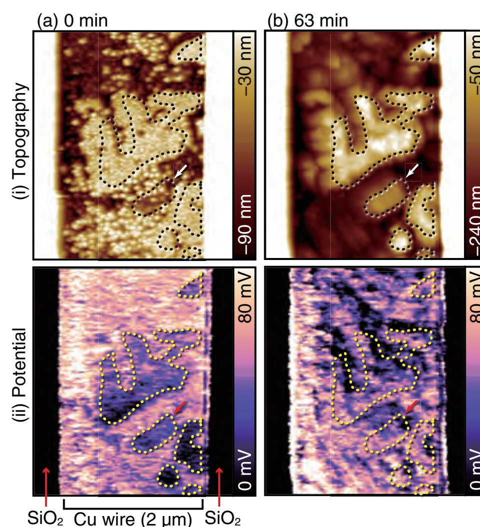

Figure 3: Topographic and potential images of a 2 μm Cu wire obtained by OL-EPM in 10 μM NaCl solution ($V_{ac} = 0.3$ V, $f_1 = 700$ kHz, $f_2 = 730$ kHz). 0 min corresponds to the time we started to image this area. 0 nm in the height scale approximately corresponds to the average height of the insulating regions made of SiO_2. For ease of comparison, we indicated the lower-potential areas observed at 0 min by dotted lines in all the images.

to the SiO_2 layer while the center showing nanoscale contrast variations corresponds to the Cu wire.

At 0 min, i.e., the time we started to image this area, the topographic image already showed nanoscale height variations (Figure 3a(i)). This is due to corrosion that occurred during the sample preparation and the tip approach and alignment processes. The simultaneously obtained potential image also shows nanoscale contrast variations (Figure 3a(ii)). We indicated some of the regions with a lower potential by dotted lines. For ease of comparison, we also reproduced the same dotted lines in all the other images in Figure 3. Comparing the topographic and potential images obtained at 0 min, we found that the lower-potential regions mostly correspond to topographically protruding areas. However, this correspondence is not perfect. For example, the area indicated by an arrow has a lower potential but is topographically depressed. This disagreement suggests that the observed potential contrasts cannot be explained by crosstalk between the topography and potential, which is a typical artifact often observed in AFM-based surface property measurements.

At 63 min, the topographic image (Figure 3b(i)) shows much clearer contrasts than the one obtained at 0 min owing to the partial dissolution of the Cu surface. At this time, the topographically protruding areas do not show a clear correspondence to the simultaneously obtained potential image (Figure 3b(ii)). However, they show a clear correspondence to the lower-potential areas observed at 0 min in spite of the 63 min time lag. These results show that the higher-potential areas dissolve much faster and hence correspond to anodic areas (corrosion sites), while the lower-potential areas correspond to cathodic areas.

Previous studies using AFM, STM and electron backscatter diffraction (EBSD) showed that the corrosion activity of polycrystalline Cu in a chloride solution strongly depends on the crystallographic orientation.[19,30,31] In 10 μM NaCl solution, corrosion progresses by the following two oxidation reactions.

$$\mathrm{Cu} \rightleftharpoons \mathrm{Cu}^{2+} + 2\mathrm{e}^- \quad (1)$$

$$\mathrm{Cu} + 2\mathrm{Cl}^- \rightleftharpoons \mathrm{CuCl}_2^- + \mathrm{e}^- \quad (2)$$

Note that reaction (2) progresses either directly or through an intermediate state such as Cu_2O or CuCl, but here we described them by a simplified reaction formula.

The Cu surface is covered with a thin layer of Cu_2O at the initial stage of surface oxidation.[32–37] Through the defects in the oxide layer, ions and charges are transferred and reactions (1) and (2) take place.[18] Meanwhile, reaction (2) takes place at the surface of the oxide layer. Owing to the higher defect density of an oxide layer on a Cu(001) surface,[19] it shows higher corrosion activity than Cu(111) and Cu(110) surfaces in 10 μM NaCl solution. Thus, the observed difference in the dissolution rate originates from the crystallographic orientation of the grains constituting the Cu wires. Both oxidation reactions (1) and (2) produce electrons in the Cu electrode and increase the cation density or decrease the anion density in the solution near the surface.

The electrons produced by the oxidation reactions are transferred to another interfacial

1
2
3
4
5
6
7
8
9
10
11
12
13
14
15
16
17
18
19
20
21
22
23
24
25
26
27
28
29
30
31
32
33
34
35
36
37
38
39
40
41
42
43
44
45
46
47
48
49
50
51
52
53
54
55
56
57
58
59
60

area and consumed by the following two reduction reactions.[18]

$$O_2 + 2H_2O + 4e^- \rightleftharpoons 4OH^- \quad (3)$$

$$2H^+ + 2e^- \rightleftharpoons H_2 \quad (4)$$

In this study, we used neutral water without removing the dissolved O_2 to prepare the solution. Thus, reaction (3) should predominantly take place. In either case, the reaction consumes electrons and increases the anion density or reduces the cation density in the solution near the surface.

As a result of these redox reactions, the relative cation density near an anodic area increases while the relative anion density increases near a cathodic area. Therefore, the anodic and cathodic areas were visualized with a higher and lower potential by OL-EPM, respectively. These results demonstrate that we can visualize the nanoscale distribution of local corrosion cells by OL-EPM.

Figures 4a-e show time-dependent changes in the topographic and potential images of Cu wires measured in 10 μM NaCl solution by OL-EPM. All the images are shown with the same height or potential scale for ease of comparison. The topographic images show that the overall height of the Cu surface decreases with time due to dissolution. However, the dissolution rate has a strong site dependence. For example, areas 1 and 2 indicated by arrows initially have a similar height to the surrounding area (Figure 4a(i)). After 120 min, these areas are lower, suggesting their higher dissolution rate. Such regions with a higher dissolution rate have a relatively high potential at 0 min (Figure 4a(ii)). This relationship between the potential and corrosion activity is consistent with that observed in Figure 3.

The potential images show that the nanoscale potential distribution markedly changes with time. At 0 min, a potential difference exists between different areas in the Cu wires (Figure 4a(ii)). However, the potential at the center of the wires gradually decreases while that at the edges remains almost the same or slightly increases. At 120 min, the greatest

1
2
3
4
5
6
7
8
9
10
11
12
13
14
15
16
17
18
19
20
21
22
23
24
25
26
27
28
29
30
31
32
33
34
35
36
37
38
39
40
41
42
43
44
45
46
47
48
49
50
51
52
53
54
55
56
57
58
59
60

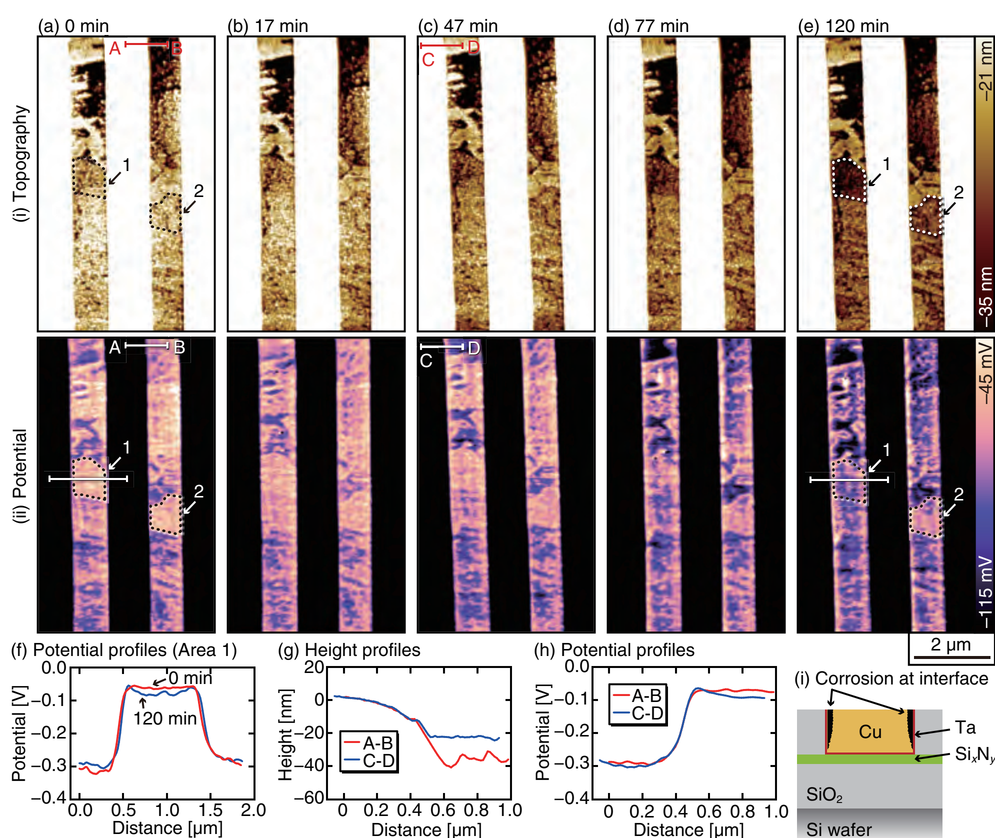

Figure 4: (a-e) Topographic and potential images of 1 μm Cu wires obtained by OL-EPM in 10 μM NaCl solution ($V_{\mathrm{ac}} = 0.5$ V, $f_1 = 700$ kHz, $f_2 = 730$ kHz). 0 min corresponds to the time we started to image this area. 0 nm in the height scale approximately corresponds to the average height of the insulating regions made of SiO_2. (f) Potential profiles measured along the lines across area 1 indicated in (a) and (e). (g, h) Height and potential profiles measured along lines A-B and C-D indicated in (a) and (c), respectively. The bars indicated at both ends of the lines show the averaging width used to take the profiles. (i) Schematic illustration of galvanic corrosion at an interface between a Cu wire and a Ta layer.

1 2 3 4 5 6 7 8 9 10 11 12 13 14 15 16 17 18 19 20 21 22 23 24 25 26 27 28 29 30 31 32 33 34 35 36 37 38 39 40 41 42 43 44 45 46 47 48 49 50 51 52 53 54 55 56 57 58 59 60

potential difference is between the edges and the center of the wires. For example, the potential of area 1 gradually decreases with time and reaches almost the same value as that of the surrounding area at 120 min. The potential profile (Figure 4f) measured across area 1 shows a decrease in potential at the center of this area.

In general, irregular contrasts at step edges can be caused by crosstalk between the topography and potential in AFM-based surface potential measurements. In this experiment, the step height at the wire edges gradually increased with time owing to the dissolution of the wires. Thus, one might consider that the enhanced potential at the wire edges was caused by an increase in the step height. However, in this experiment, we cannot explain the observed contrasts by such an artifact for the following reason. The height profiles in Figure 4g show that the step height along line A-B ($\sim$35 nm) is larger than that along line C-D ($\sim$20 nm). Meanwhile, the potential profiles in Figure 4h show that the potential at the wire edge is enhanced only along line C-D, where we see a lower step height. This result shows that a larger step height does not necessarily give an enhancement of potential at the wire edges.

At the wire edges, a 25 nm Ta layer is inserted between the Cu and SiO_2 regions. The Cu/Ta contact leads to the formation of galvanic corrosion cells.[38,39] In addition, the crystallinity of the Cu wires near the interface is lower than that at the center. These factors accelerate corrosion at the interface to form a line-shaped crevice along the wire edges as shown in Figure 4i. So far, such corrosion of Cu wire edges has been confirmed by ex-situ SEM measurements.[29] However, in-situ measurements of such a corrosion process have been difficult even by AFM or STM. For example, it is almost impossible to discuss when the corrosion reactions at the wire edges took place from the topographic images shown in Figure 4. In contrast, the potential images clearly show the real-time transition of the corrosion sites and hence the corrosion mechanism. These results demonstrate the effectiveness of the real-time visualization of local corrosion cells for understanding the nanoscale corrosion mechanism.

1
2
3
4
5
6
7
8
9
10
11
12
13
14
15
16
17
18
19
20
21
22
23
24
25
26
27
28
29
30
31
32
33
34
35
36
37
38
39
40
41
42
43
44
45
46
47
48
49
50
51
52
53
54
55
56
57
58
59
60

Corrosion of duplex stainless steel

Duplex stainless steel consists of ferrite (α) and austenite (γ) phases, typically with a 1:1 ratio.[40] Owing to its high corrosion resistance, it is used as a construction material for large-scale plants operating in severely corrosive environments, such as nuclear power, desalination and chemical plants. To optimize the corrosion resistance in different environments, various types of stainless steel have been developed.[41] In the development process, evaluation of the local corrosion resistance has been a serious problem. Owing to the high corrosion resistance of stainless steel, it can take more than a few months to induce surface structural changes by corrosion. Thus, ex-situ measurement by SEM or in-situ imaging by AFM or STM is often inefficient or impossible. To solve this problem, there has been strong demand for a method of evaluating the nanoscale distribution of local corrosion resistance in a typical experimental time (i.e., several hours).

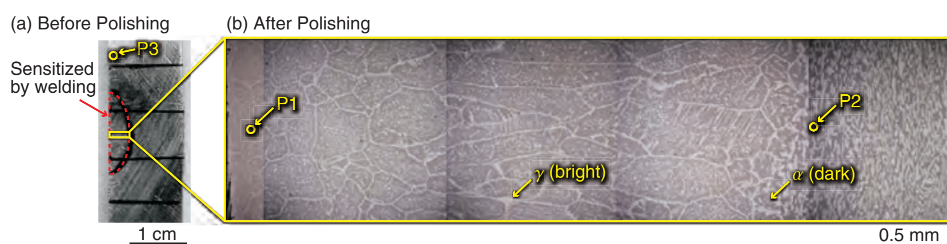

Figure 5: Optical micrographs of the duplex stainless-steel sample used in this study. (a) Large-scale view before polishing. The area indicated by dotted lines is sensitized by welding. (b) Magnified view at the position indicated by the rectangle in (a) after polishing. We performed OL-EPM measurements at positions P1-P3.

In this study, we investigate the corrosion processes of duplex stainless steel (UNS S32750) in an electrolytic solution by OL-EPM. This material has a high corrosion resistance under various solution conditions. However, when it is welded, the surrounding area is sensitized to show a degraded corrosion resistance.[40,42] Such degradation by welding is one of the major problems in the applications of duplex stainless steels. To understand the influence of welding, here we investigate the nanoscale corrosion behavior of a sensitized stainless steel.

Figure 5a shows an optical micrograph of the sample used in this experiment before

1
2
3
4
5
6
7
8
9
10
11
12
13
14
15
16
17
18
19
20
21
22
23
24
25
26
27
28
29
30
31
32
33
34
35
36
37
38
39
40
41
42
43
44
45
46
47
48
49
50
51
52
53
54
55
56
57
58
59
60

polishing. The area surrounded by dotted lines is sensitized by welding. Figure 5b shows a magnified optical micrograph taken after polishing at the position indicated by the rectangle in Figure 5a. In the image, the darker contrast corresponds to α-phase grains while the brighter contrast corresponds to γ-phase grains. The image shows that the size of α-phase grains is significantly enlarged by the welding. We performed OL-EPM measurements at locations with different distances from the weld as indicated by arrows P1-P3.

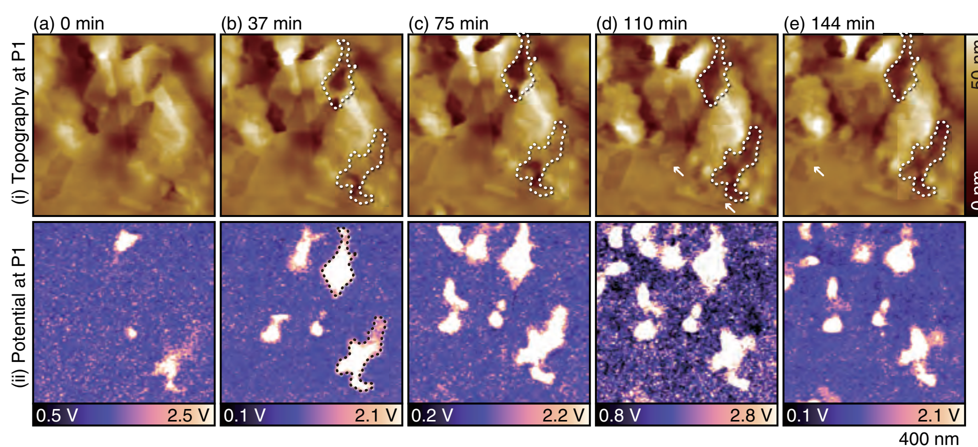

Figure 6: Topographic and potential images of the sensitized duplex stainless steel obtained in 10 mM NaCl solution at P1 indicated in Figure 5b (V_{ac} = 1 V, f_1 = 700 kHz, f_2 = 730 kHz). 0 min corresponds to the time we started to image this area. 0 nm in the topographic images is arbitrary.

Figure 6 shows topographic and potential images of the sensitized duplex stainless steel obtained in 10 mM NaCl solution at P1 indicated in Figure 5b. The potential images show much clearer nanoscale contrasts than those observed in the images of the Cu wires (Figures 3 and 4). These potential contrasts do not necessarily correspond to the structural features observed in the topographic images. Thus, the potential contrasts cannot be explained only by crosstalk between the topography and potential.

Comparing the topographic and potential images, we found that the areas showing a higher potential selectively dissolve to form depressions. For example, areas indicated by dotted lines in the potential image obtained at 37 min (Figure 6b(ii)) show a higher potential than the surrounding areas. The same dotted lines are overlaid on the topographic images

in Figures 6b-e. At 37 min, the topographic features do not show a clear correspondence to the higher-potential areas. However, these areas gradually dissolve to form depressions. At 144 min, the depressed areas show excellent agreement with the higher-potential areas in spite of the 107 min time lag. This is consistent with the results obtained with the Cu wires.

A stainless-steel surface is typically covered with a thin chromium oxide layer, which acts as a passive layer and gives excellent corrosion resistance.[40] However, when it is welded, the σ phase and chromium carbides and nitrides are formed near the grain boundaries.[42] This produces local areas where the Cr concentration is insufficient to form a passive layer. Such areas act as an anode, where the following oxidation reaction takes place.

$$\mathrm{Fe} \rightleftharpoons \mathrm{Fe}^{2+} + 2\mathrm{e}^{-} \tag{5}$$

Owing to an increase in the density of cations (i.e., Fe^{2+}), the potential in the solution near the anodic areas increases.

Meanwhile, all the other areas covered with a passive layer act as a cathode, where reduction reactions (3) and (4) take place. These reactions increase the relative anion density and lower the potential in the solution near the cathodic areas. Therefore, the corrosion sites show a higher potential than the surrounding areas. This is consistent with the discussion on the corrosion of the Cu wires.

Owing to the excellent corrosion resistance of a chromium oxide layer, the separation between the anodic and cathodic areas is much clearer than that in the corrosion of the Cu wires. Thus, the corrosion of stainless steel is very localized and forms deep pits, which is known as pitting corrosion.[43–48] This explains the clearer potential contrasts compared with those observed in the corrosion of the Cu wires (Figures 3 and 4).

In addition to the dissolution, we found the formation of layer-like structures with a thickness of 2–4 nm as indicated by arrows in Figures 6d and 6e. They are most likely to be corrosion products of Fe.[6] In general, the corrosion of Fe produces Fe^{2+} and OH^{-} to form

$Fe(OH)_2$. $Fe(OH)_2$ reacts with dissolved oxygen to form $Fe(OH)_3$. Through dehydration, these hydroxides become various oxides such as FeO, Fe_3O_4 and Fe_2O_3, and their hydrates. These oxides form layer-like structures on the Fe surface, which is known as rust. The deposition or growth of these corrosion products does not involve redox reactions; thus, the potential images show no contrast changes corresponding to these events.

These results suggest that the surface of this imaging area is mostly covered with oxide layers and that corrosion mainly takes place under them. For example, between 75 min and 110 min, the surface layer at the location indicated by dotted lines suddenly disappears to produce a depression. However, this is the cumulative result of the corrosion reaction underneath the oxide layer. In fact, such corrosion activity is visualized in the potential images obtained much earlier than when the structural changes occur. This demonstrates the unique capability of OL-EPM to predict corrosion sites well in advance of structural changes.

Using this capability, we have investigated the local corrosion resistance at positions far from the weld, where no structural changes are observed within a typical experimental time even in an acidic solution (pH 3). At P2, i.e., around the edge of the sensitized area, nanoscale pits are formed as shown in Figure 7a. However, we found no changes in the width and depth ($\sim$10 nm) for more than 100 min. Meanwhile, the potential image (Figure 7b) shows that these pits have a higher potential than the surrounding area, suggesting higher corrosion activity.

At P3, i.e., far from the weld, the topographic image (Figure 7c) shows the existence of many protrusions with a height of 1–3 nm. We were not able to observe any structural changes during the experimental time. The potential image (Figure 7d) shows a clear contrast between the upper left and lower right regions. The height profile (Figure 7e) across the boundary between the two regions shows the existence of a height difference of $\sim$0.5 nm. This height difference is not small compared with the vertical resolution of AFM (< 10 pm). However, owing to the existence of protrusions, it is difficult to see it in the topographic

1
2
3
4
5
6
7
8
9
10
11
12
13
14
15
16
17
18
19
20
21
22
23
24
25
26
27
28
29
30
31
32
33
34
35
36
37
38
39
40
41
42
43
44
45
46
47
48
49
50
51
52
53
54
55
56
57
58
59
60

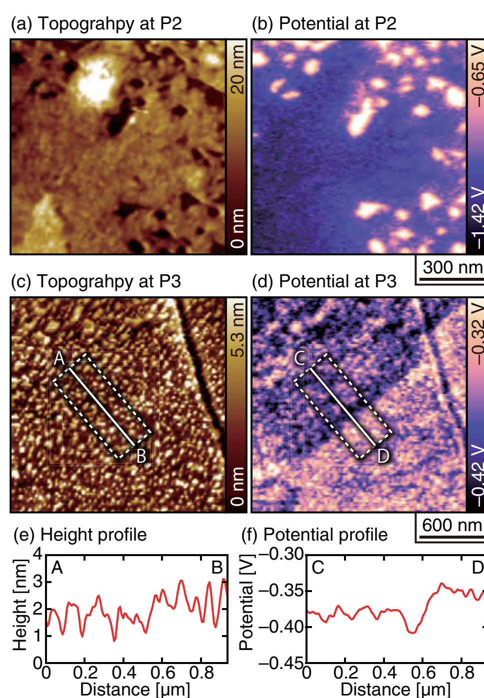

Figure 7: Topographic and potential images of the sensitized duplex stainless steel obtained in acidic solution of pH 3 at (a, b) P2 and (c, d) P3 indicated in Figure 5 (V_{ac} = 0.8 V, f_1 = 700 kHz, f_2 = 730 kHz). 0 nm in the topographic images is arbitrary. (a, b) Solution contains 1 mM HCl and 1 mM NaCl. (c, d) Solution contains 1 mM HCl.

1 2 3 4 5 6 7 8 9 10 11 12 13 14 15 16 17 18 19 20 21 22 23 24 25 26 27 28 29 30 31 32 33 34 35 36 37 38 39 40 41 42 43 44 45 46 47 48 49 50 51 52 53 54 55 56 57 58 59 60

image. In contrast, we can clearly see this boundary in the potential profile as shown in Figure 7f.

As a γ-phase grain is mechanically softer than an α-phase grain, it is slightly depressed after polishing. Thus, the upper left and lower right regions correspond to γ- and α-phase grains, respectively. This result suggests that an α-phase grain near a grain boundary has a higher corrosion activity than the surrounding area, although the difference is much smaller than that observed in Figures 6 and 7b. Such a potential difference between the two phases does not exist everywhere near the boundaries and exists only at local spots. Thus, it is likely that the difference in corrosion resistance originates from the local variation of the compositional ratio near the grain boundaries. So far, evaluation of the local corrosion resistance of stainless steel has been a serious problem owing to its high corrosion resistance. The examples shown here demonstrate that OL-EPM enables such evaluation in a relatively short time even without changes in surface structures.

Conclusions

In this study, we have investigated the nanoscale corrosion behavior of Cu fine wires and stainless steel by the in-situ imaging of local corrosion cells by OL-EPM.

We have demonstrated the capability of OL-EPM to visualize the nanoscale distribution of local corrosion cells. The higher-potential and lower potential areas correspond to anodic areas (i.e., corrosion sites) and cathodic areas, respectively. We experimentally confirmed this correspondence for the corrosion of two different materials (i.e., Cu and stainless steel) and explained it by an increase in the relative cation density in the solution near the anode and the relative anion density near the cathode. Owing to the generality of this explanation, it should also be true for other corrosion processes.

The direct imaging of local corrosion cells plays two important roles in corrosion research. First, it reveals the real-time transition of local corrosion sites. Many corrosion processes

1
2
3
4
5
6
7
8
9
10
11
12
13
14
15
16
17
18
19
20
21
22
23
24
25
26
27
28
29
30
31
32
33
34
35
36
37
38
39
40
41
42
43
44
45
46
47
48
49
50
51
52
53
54
55
56
57
58
59
60

take place under the topmost surface owing to the existence of oxide layers and other corrosion products. Thus, structural changes that we can observe by AFM often fail to provide real-time information on corrosion sites. In contrast, the potential immediately responds to corrosion reactions and hence provides more instantaneous information. Secondly, it enables the local corrosion resistance of highly corrosion-resistant materials to be evaluated in a relatively short time. This capability will help to dramatically reduce the time and cost required for testing the local corrosion resistance of stainless steels, accelerating their development.

With the above capabilities, we obtained important findings on the corrosion mechanism. In the corrosion of the Cu fine wires, we found that local corrosion cells are initially formed between grains with different crystallographic orientations but later between the center and edges of the wires. For the corrosion of the sensitized duplex stainless steel, we experimentally confirmed that local corrosion cells indeed exist even when the surface structure does not show any detectable changes. These findings demonstrate the effectiveness of the proposed method for studying corrosion. In principle, the imaging capability of anodic and cathodic areas should also be useful for investigating other redox reactions on a battery electrode or a catalytic material. The results presented here open up such future applications of OL-EPM in nanoscale electrochemistry.

Methods

OL-EPM measurements

In this study, we obtained topographic and potential images by OL-EPM operated in the dual-frequency mode (DF-OL-EPM). Detailed explanations of the principle and experimental setup were reported previously.[22–24] Thus, here we give a brief summary and the operating conditions used in this study. In DF-OL-EPM, a sum of two sine waves, $V_{\mathrm{ac}} \cos \omega_1 t$ and $V_{\mathrm{ac}} \cos \omega_2 t$, is applied between a tip and a sample. This induces cantilever vibration at various frequencies. Among them, we detect the ω_1 and $\omega_{\mathrm{L}} (= |\omega_1 - \omega_2|)$ components from

ACS Paragon Plus Environment

1 2 3 4 5 6 7 8 9 10 11 12 13 14 15 16 17 18 19 20 21 22 23 24 25 26 27 28 29 30 31 32 33 34 35 36 37 38 39 40 41 42 43 44 45 46 47 48 49 50 51 52 53 54 55 56 57 58 59 60

a cantilever deflection signal using a lock-in amplifier. From the obtained parameters, the local potential V_s is calculated by the following equation:

$$V_\mathrm{s} = \mathrm{sgn}(\cos\phi_1)\frac{A_1/G(\omega_1)}{A_\mathrm{L}/G(\omega_\mathrm{L})}\frac{V_\mathrm{ac}}{2}, \quad (6)$$

where A_1 and ϕ_1 are the amplitude and phase of the ω_1 component, respectively, while A_L is the amplitude of the ω_L component of the cantilever deflection signal. $G(\omega)$ is the transfer function of the cantilever response.

In this study, we used a custom-built AFM instrument with an ultralow noise cantilever deflection sensor[49,50] and a highly stable photothermal cantilever excitation system.[51,52] The tip–sample distance was regulated such that the cantilever oscillation amplitude was kept constant. A commercially available AFM controller (RC4/OC4, SPECS) was used for the OL-EPM operation. Si cantilevers (AC55, Olympus) having a nominal spring constant of ∼85 N/m, a typical resonance frequency of ∼1.3 MHz and a Q factor of ∼12 in an aqueous solution were used. These cantilevers came with a Au backside coating but we coated their front side with a 30 nm Au film using a dc sputter coater (K575XD, Emitech). An ac bias voltage was produced by adding a sine wave $V_\mathrm{ac}\cos\omega_2 t$ from a function generator (AFG3022B, Tektronix) to another sine wave $V_\mathrm{ac}\cos\omega_1 t$ from a lock-in amplifier (HF2LI: Zurich Instruments). A_1, A_L and ϕ_1 were detected from a cantilever deflection signal using the same lock-in amplifier. All the OL-EPM measurements were performed at room temperature. The imaging parameters such as V_ac, $f_1(=\omega_1/2\pi)$ and $f_2(=\omega_2/2\pi)$ are given in the figure captions.

Preparation of the Cu fine wire samples

We used patterned Cu fine wires fabricated on a Si wafer (854 Cu CMPd Wafer, Advanced Materials Technology) as shown in Figures 2a-c. As illustrated in Figure 2d, the Cu wires were formed on a 25 nm Ta film and had a thickness of 475 nm. An outline of the fabrication

process is as follows. (1) Patterned trench structures were formed by etching the SiO_2 layer on the Si wafer. (2) A 25 nm Ta film was formed on the wafer surface by physical vapor deposition. (3) A thick Cu film was formed on the Ta film by electroplating. (4) The wafer was annealed at 150°C for 30 min. (5) The surface was polished by CMP to reduce the SiO_2 thickness to 500 nm, which corresponds to a Cu wire thickness of 475 nm. In this way, polycrystalline Cu fine wires were fabricated. The wires consisted of nanoscale grains with different crystallographic orientations. For the AFM measurements, we cut the wafer into pieces with a size of 10 mm $\times$ 10 mm.

To remove surface contaminants, we cleaned the surface using an Ar plasma cleaner (SC-701, Sanyu Electronics). We found that the Ar plasma cleaning under typical operating conditions can severely damage the Cu wires. Thus, we adjusted the bias voltage and inlet gas pressure to the minimum values required to maintain the plasma. In addition, we covered the sample with a Cu plate to suppress the electric field applied to the sample surface. Under these conditions, the damage of the wires caused by the cleaning was negligible.

After the Ar plasma cleaning, we attached the sample to a sample holder for our AFM system. On the fixed sample, we added dropwise 100 μL 0.5 M citric acid solution and left the sample for 1 min to remove organic contaminants deposited on the surface during the sample transfer process. Subsequently, we exchanged the deposited solution with pure water by gentle pipetting. We repeated this process five times not only to completely replace the solution but also to rinse the surface with pure water.

We set the sample holder onto our AFM system. Immediately before starting the coarse approach of the tip, we replaced the water on the sample with an imaging solution, i.e., 10 μM NaCl solution. We repeated this process twice to completely replace the solution with the imaging solution.

1
2
3
4
5
6
7
8
9
10
11
12
13
14
15
16
17
18
19
20
21
22
23
24
25
26
27
28
29
30
31
32
33
34
35
36
37
38
39
40
41
42
43
44
45
46
47
48
49
50
51
52
53
54
55
56
57
58
59
60

Preparation of duplex stainless-steel samples

We used UNS S32750 duplex stainless steel, which contains Cr (24.6 wt.%), Ni (5.85 wt.%), Mo (1.56 wt.%), Mn (1.15 wt.%), Si (0.69 wt.%), N (0.23 wt.%), Cu (0.19 wt.%), P (0.03 wt.%), C (0.02 wt.%) and S (0.001 wt.%). At the center of a large stainless-steel plate, we applied bead-on-plate gas tungsten arc welding (GTAW) to form a line-shaped sensitized area. The GTAW machine was operated with a travel speed of 100 mm/min, arc current of 300 A and arc voltage of 17 V. After the welding, we cut the plate perpendicularly to the welded surface and obtained a cross-sectional slice with a thickness of 1.5 mm. An optical micrograph of this cross-sectional surface is shown in Figure 5a. We further cut it into pieces with a size of 12 mm $\times$ 8 mm $\times$ 1.5 mm and imaged two of them. One was located at the center of the weld while the other was away from it as shown in Figure 5a.

The surface of the sample was polished by a polishing machine (TegraPol-11, Struers). We polished the surface with No. 80, 120, 240, 400, 600, 800, 1000, 1200, 1500 and 2000 emery papers for 3 min each. We further polished the surface with suspensions referred to as Blue, Red and Diamond purchased from Struers for 6–12 min each. Finally, we polished the surface for 2 min with an active oxide polishing suspension (OP-U, Struers) after dilution by a factor of two. For all the polishing processes, we used a rotation speed of 150 rpm and a loading force of 15 N. After each of the polishing processes, we performed 5 min ultrasonication to clean the surface.

Just before imaging, we cleaned the surface using Ar plasma cleaner (SC-701, Sanyu Electronics). Immediately after the cleaning, the sample was glued to a sample holder for our AFM system. An electrical contact with the sample was formed by attaching a Cu thin wire to the sidewall of the sample with silver paste. We deposited 100 μL of imaging solution on the sample surface and performed OL-EPM imaging in it.

ACS Paragon Plus Environment

1
2
3
4
5
6
7
8
9
10
11
12
13
14
15
16
17
18
19
20
21
22
23
24
25
26
27
28
29
30
31
32
33
34
35
36
37
38
39
40
41
42
43
44
45
46
47
48
49
50
51
52
53
54
55
56
57
58
59
60

Preparation of imaging solution

We used 0.01, 1 and 10 mM NaCl aqueous solutions for the imaging experiments. All the solutions were prepared by dissolving powder form NaCl (31320-05, Nacalai Tesque) in ultrapure water (Milli-Q Element A10). For the images shown in Figure 7, we lowered the pH of the solution to 3 by adding 0.1 M HCl solution (18321-05, Nacalai Tesque). This approximately corresponds to a HCl concentration of 1 mM in the obtained imaging solution.

Acknowledgement

This work was supported by ACT-C, Japan Science and Technology Agency.

References

1. Shintaku, Y.; Iwamatsu, F.; Suga, K.; Wada, Y.; Kikuchi, M. Simulation of Stress Corrosion Cracking in In-Core Monitor Housing of Nuclear Power Plant. *J. Press. Vess-T. ASME* **2015**, *137*, 041401.

2. Marangou, V. S.; Sawides, K. First Desalination Plant in Cyprus - Product Water Aggresivity and Corrosion Control. *Desalination* **2001**, *138*, 251–258.

3. Anderko, A.; Sridhar, N.; Yang, L. T.; Grise, S. L.; Saldanha, B. J.; Dorsey, M. H. Validation of Localised Corrosion Model Using Real Time Corrosion Monitoring in a Chemical Plant. *Corros. Eng. Sci. Techn.* **2005**, *40*, 33–42.

4. Kodera, M.; Uekusa, S.-I.; Nagano, H.; Tokushige, K.; Shima, S.; Fukunaga, A.; Mochizuki, Y.; Fukuda, A.; Hiyama, H.; Tsujimura, M. Stress Corrosion Cracking of Cu Interconnects During CMP with a Cu/Porous Low-k Structure. *J. Electrochem. Soc.* **2005**, *152*, G506–G510.

5. Pardo, A.; Merino, M. C.; Coy, A. E.; Arrabal, R.; Viejo, F.; Matykina, E. Corrosion

Behaviour of Magnesium/Aluminium Alloys in 3.5 wt.% NaCl. *Corros. Sci.* **2008**, *50*, 823–834.

6. Revie, R. W.; Uhlig, H. H. *Corrosion and Corrosion Control - An Introduction to Corrosion Science and Engineering 4th Ed.*; Wiley-Interscience, 2008.

7. Zhao, X. J.; Zhu, G.; Fan, Y. J.; Li, H. Y.; Wang, Z. L. Triboelectric Charging at the Nanostructured Solid/Liquid Interface for Area-Scalable Wave Energy Conversion and Its Use in Corrosion Protection. *ACS Nano* **2015**, *9*, 7671–7677.

8. Zhou, F.; Li, Z.; Shenoy, G. J.; Li, L.; Liu, H. Enhanced Room-Temperature Corrosion of Copper in the Presence of Graphene. *ACS Nano* **2013**, *7*, 6939–6947.

9. Duarte, M. J.; Klemm, J.; Klemm, S. O.; Mayrhofer, K. J. J.; Stratmann, M.; Borodin, S.; Romero, A. H.; Madinehei, M.; Crespo, D.; Serrano, J.; Gerstl, S. S. A.; Choi, P. P.; Raabe, D.; Renner, F. U. Element-Resolved Corrosion Analysis of Stainless-Type Glass-Forming Steels. *Science* **2013**, *341*, 372–376.

10. Borisova, D.; Möhwald, H.; Shchukin, D. G. Mesoporous Silica Nanoparticles for Active Corrosion Protection. *ACS Nano* **2011**, *5*, 1939–1946.

11. Skorb, E. V.; Skirtach, A. G.; Sviridov, D. V.; Shchukin, D. G.; Möhwald, H. Laser-Controllable Coatings for Corrosion Protection. *ACS Nano* **2009**, *3*, 1753–1760.

12. King, A.; Johnson, G.; Engelberg, D.; Ludwig, W.; Marrow, J. Observations of Intergranular Stress Corrosion Cracking in a Grain-Mapped Polycrystal. *Science* **2008**, *321*, 382–385.

13. Ryan, M. P.; Williams, D. E.; Chater, R. J.; Hutton, B. M.; McPhail, D. S. Why Stainless Steel Corrodes. *Nature* **2002**, *415*, 770–774.

14. Newman, R. C.; Sieradzki, K. Metalic Corrosion. *Science* **1994**, *263*, 1708–1709.

15. Oppenheim, I. C.; Trevor, D. J.; Chidsey, C. E. D.; Trevor, P. L.; Sieradzki, K. In Situ Scanning Tunneling Microscopy of Corrosion of Silver-Gold Alloys. *Science* **1991**, *254*, 687–689.

16. Hsieh, Y.-P.; Hofmann, M.; Chang, K.-W.; Jhu, J. G.; Li, Y.-Y.; Chen, K. Y.; Yang, C. C.; Chang, W.-S.; Chen, L.-C. Complete Corrosion Inhibition through Graphene Defect Passivation. *ACS Nano* **2014**, *8*, 443–448.

17. Renner, F. U.; Stierle, A.; Dosch, H.; Kolb, D. M.; Lee, T.-L.; Zegenhagen, J. Initial Corrosion Observed on the Atomic Scale. *Nature* **2006**, *439*, 707–710.

18. Kear, G.; Barker, B. D.; Walsh, F. C. Electrochemical Corrosion of Unalloyed Copper in Chloride Media - A Critical Review. *Corros. Sci.* **2004**, *46*, 109–135.

19. Martinez-Lombardia, E.; Gonzalez-Garcia, Y.; Lapeire, L.; Graeve, I. D.; Verbeken, K.; Kestens, L.; Mol, J. M. C.; Terryn, H. Scanning Electrochemical Microscopy to Study the Effect of Crystallographic Orientation on the Electrochemical Activity of Pure Copper. *Electrochimica Acta* **2014**, *116*, 89–96.

20. Nonnenmacher, M.; O'Boyle, M. P.; Wickramasinghe, H. K. Kelvin Probe Force Microscopy. *Appl. Phys. Lett.* **1991**, *58*, 2921–2923.

21. Kitamura, S.; Iwatsuki, M. High-Resolution Imaging of Contact Potential Difference with Ultrahigh Vacuum Noncontact Atomic Force Microscopy. *Appl. Phys. Lett.* **1998**, *72*, 3154–3156.

22. Kobayashi, N.; Asakawa, H.; Fukuma, T. Nanoscale Potential Measurements in Liquid by Frequency Modulation Atomic Force Microscopy. *Rev. Sci. Instrum.* **2010**, *81*, 123705.

23. Kobayashi, N.; Asakawa, H.; Fukuma, T. Quantitative Potential Measurements of Nanoparticles with Different Surface Charges in Liquid by Open-Loop Electric Potential Microscopy. *J. Appl. Phys.* **2011**, *110*, 044315.

24. Kobayashi, N.; Asakawa, H.; Fukuma, T. Dual Frequency Open-Loop Electric Potential Microscopy for Local Potential Measurements in Electrolyte Solution with High Ionic Strength. *Rev. Sci. Instrum.* **2012**, *83*, 033709.

25. Umeda, K.-I.; Kobayashi, K.; Oyabu, N.; Hirata, Y.; Matsushige, K.; Yamada, H. Analysis of Capacitive Force Acting on a Cantilever Tip at Solid/Liquid Interfaces. *J. Appl. Phys.* **2013**, *113*, 154311.

26. Umeda, K.-I.; Kobayashi, K.; Oyabu, N.; Hirata, Y.; Matsushige, K.; Yamada, H. Practical Aspects of Kelvin-Probe Force Microscopy at Solid/Liquid Interfaces in Various Liquid Media. *J. Appl. Phys.* **2014**, *116*, 134307.

27. Collins, L.; Jesse, S.; Kilpatrick, J. I.; Tselev, A.; Varenyk, O.; Okatan, M. B.; Weber, S. A. L.; Kumar, A.; Balke, N.; Kalinin, S. V.; Rodriguez, B. J. Probing Charge Screening Dynamics and Electrochemical Processes at the Solid-Liquid Interface with Electrochemical Force Microscopy. *Nat. Comm.* **2014**, *5*, 38971.

28. Collins, L.; Jesse, S.; Kilpatrick, J. I.; Tselev, A.; Okatan, M. B.; Kalinin, S. V.; Rodriguez, B. J. Kelvin Probe Force Microscopy in Liquid Using Electrochemical Force Microscopy. *Beilstein. J. Nanotechnol.* **2015**, *6*, 201–214.

29. Yamada, Y.; Konishi, N.; Noguchi, J.; Jimbo, T. Influence of CMP Slurries and Post-CMP Cleaning Solutions on Cu Interconnects and TDDB Reliability. *J. Electrochem. Soc.* **2008**, *155*, H485–H490.

30. Lapeire, L.; Martinez-Lombardia, E.; Verbeken, K.; Graeve, I. D.; Kestens, L. A. I.; Terryn, H. Effect of Neighboring Grains on the Microscopic Corrosion Behavior of a Grain in Polycrystalline Copper. *Corros. Sci.* **2013**, *67*, 179–183.

31. Martinez-Lombardia, E.; Maurice, V.; Lapeire, L.; Graeve, I. D.; Verbeken, K.; Kestens, L.; Marcus, P.; Terryn, H. In Situ Scanning Tunneling Microscopy Study of

ACS Paragon Plus Environment

Grain-Dependent Corrosion on Microcrystalline Copper. *J. Phys. Chem. C* **2014**, *118*, 25421–25428.

32. Wieder, H.; Canderna, A. W. The Oxidation of Copper Films to $CuO_{0.67}$. *J. Phys. Chem.* **1962**, *66*, 816–821.

33. Tajima, N.; Fukui, M.; Shintani, Y.; Tada, O. In Situ Studies on Oxidation of Copper Films by Using ATR Technique. *J. Phys. Soc. Jap.* **1985**, *54*, 4236–4240.

34. Itoh, J.; Sasaki, T.; Ohtsuka, T. The Influence of Oxide Layers on Initial Corrosion Behavior of Copper in Air Containing Water Vapor and Sulfur Dioxide. *Corros. Sci.* **2000**, *42*, 1539–1551.

35. Choi, K. S.; Kang, T. G.; Park, I. S.; Lee, J. H.; Cha, K. B. Copper Lead Frame: An Ultimate Solution to the Reliability of BLP Package. *IEEE T. Electron. Pack.* **2000**, *23*, 32–38.

36. Lim, J. W.; Iijima, J.; Zhu, Y. F.; Yoo, J. H.; Choi, G. S.; Mimura, K.; Isshiki, M. Nanoscale Investigation of Long-Term Native Oxidation of Cu Films. *Thin Solid Films* **2008**, *516*, 4040–4046.

37. Gao, J.; Hu, A.; Li, M.; Mao, D. Influence of Crystal Orientation on Copper Oxidation Failure. *Appl. Surf. Sci.* **2009**, *255*, 5943–5947.

38. Hung, C.-C.; Wang, Y.-S.; Lee, W.-H.; Chang, S.-C.; Wang, Y.-L. Galvanic Corrosion Between TaN_x Barriers and Copper Seed. *Electrochem. Solid St.* **2007**, *10*, H127–H130.

39. Hung, C.-C.; Lee, W.-H.; Wang, Y.-S.; Chang, S.-C.; Wang, Y.-L. Investigation of Galvanic Corrosion Between TaN_x Barriers and Copper Seed by Electrochemical Impedance Spectroscopy. *Electrochem. Solid St.* **2007**, *10*, D100–D103.

40. Chang, K. W.; Tjong, S. C. Effect of Secondary Phase Precipitation on the Corrosion Behavior of Duplex Stainless Steels. *Materials* **2014**, *7*, 5268–5304.

1
2
3
4
5
6
7
8
9
10
11
12
13
14
15
16
17
18
19
20
21
22
23
24
25
26
27
28
29
30
31
32
33
34
35
36
37
38
39
40
41
42
43
44
45
46
47
48
49
50
51
52
53
54
55
56
57
58
59
60

41. Lo, K. H.; Shek, C. H.; Lai, J. K. L. Recent Developments in Stainless Steels. *Mater. Sci. Eng. R.* **2009**, *65*, 39–104.

42. Karlsson, L. Welding Duplex Stainless Steel - A Review of Current Recommendations. *Weld. World* **2012**, *56*, 65–76.

43. Lopez, N.; Cid, M.; Puiggali, M. Influence of σ-Phase Precipitation on Mechanical Properties and Corrosion Resistance of Duplex Stainless Steels. *Corros. Sci.* **1999**, *41*, 1615–1631.

44. Chen, T. H.; Yang, J. R. Effects of Solution Treatment and Continuous Cooling on σ-Phase Precipitation in a 2205 Duplex Stainless Steel. *Mater. Sci. Eng. A* **2001**, *311*, 28–41.

45. Adhe, K. N.; Kain, V.; Madangopal, K.; Gadiyar, H. S. Influence of Sigma Phase Formation on the Localized Corrosion Behavior of a Duplex Stainless Steel. *J. Mater. Eng. Perform.* **1996**, *5*, 500–506.

46. Park, C. J.; Rao, V. S.; Kwon, H. S. Effect of Sigma Phase on the Initiation and Propagation of Pitting Corrosion of Duplex Stainless Steel. *Corrosion* **2005**, *61*, 76–83.

47. Ebrahimi, N.; Momeni, M.; Moayed, M. H.; Davoodi, A. Correlation between Critical Pitting Temperature and Degree of Sensitization on Alloy 2205 Duplex Stainless Steel. *Corros. Sci.* **2011**, *53*, 637–644.

48. Hong, J.; Han, D.; Tan, H.; Li, J.; Jiang, Y. Evaluation of Aged Duplex Stainless Steel UNS S32750 Susceptibility to Intergranular Corrosion by Optimized Double Loop Electrochemical Potentiokinetic Reactivation Method. *Corros. Sci.* **2013**, *68*, 249–255.

49. Fukuma, T.; Kimura, M.; Kobayashi, K.; Matsushige, K.; Yamada, H. Development of Low Noise Cantilever Deflection Sensor for Multienvironment Frequency-Modulation Atomic Force Microscopy. *Rev. Sci. Instrum.* **2005**, *76*, 053704.

ACS Paragon Plus Environment

1
2
3
4
5
6
7
8
9
10
11
12
13
14
15
16
17
18
19
20
21
22
23
24
25
26
27
28
29
30
31
32
33
34
35
36
37
38
39
40
41
42
43
44
45
46
47
48
49
50
51
52
53
54
55
56
57
58
59
60

50. Fukuma, T.; Jarvis, S. P. Development of Liquid-Environment Frequency Modulation Atomic Force Microscope with Low Noise Deflection Sensor for Cantilevers of Various Dimensions. *Rev. Sci. Instrum.* **2006**, *77*, 043701.

51. Fukuma, T. Wideband Low-Noise Optical Beam Deflection Sensor with Photothermal Excitation for Liquid-Environment Atomic Force Microscopy. *Rev. Sci. Instrum.* **2009**, *80*, 023707.

52. Fukuma, T.; Onishi, K.; Kobayashi, N.; Matsuki, A.; Asakawa, H. Atomic-Resolution Imaging in Liquid by Frequency Modulation Atomic Force Microscopy Using Small Cantilevers with Megahertz-Order Resonance Frequencies. *Nanotechnology* **2012**, *23*, 135706.

1
2
3
4
5
6
7
8
9
10
11
12
13
14
15
16
17
18
19
20
21
22
23
24
25
26
27
28
29
30
31
32
33
34
35
36
37
38
39
40
41
42
43
44
45
46
47
48
49
50
51
52
53
54
55
56
57
58
59
60

Graphical TOC Entry